Rational design of bifunctional hierarchical Pd/SAPO-5 for the synthesis of tetrahydrofuran derivatives from furfural

L. Gao [a,1], I. Miletto [b,1], C. Ivaldi [b], G. Paul [b], L. Marchese [b], S. Coluccia [c], F. Jiang [a], E. Gianotti [b,*], M. Pera-Titus [a,*]

[a] Eco-Efficient Products and Processes Laboratory (E2P2L), UMI 3464 CNRS-Solvay, 3966 Jin Du Road, Xin Zhuang Ind. Zone, 201108 Shanghai, China
[b] Department of Science and Technological Innovation, Università del Piemonte Orientale, Viale T. Michel 11, 15121 Alessandria, Italy
[c] Department of Chemistry, Università degli Studi di Torino, Via P. Giuria 7, 10125, Torino, Italy

A B S T R A C T

The one-pot aldol condensation/crotonization reaction between furfural and methyl isobutyl ketone (MIBK), followed by hydrogenation with molecular H_2, was implemented for preparing tetrahydrofuran derivatives. To this aim, we developed a robust Pd/HPSAPO-5 catalyst based on the crystalline silico-aluminophosphate SAPO-5 with hierarchical porosity and optimized silicon content. The hierarchical HPSAPO-5 catalyst was synthesized using a bottom-up method starting from pre-synthesized MCM-41, with the surfactant (CTAB) inside the mesopores, serving both as Si source and mesoporogen. NH_3-TPD and FT-IR spectroscopy of adsorbed probe molecules combined with solid-state ^1H MAS NMR were used to assess the nature, strength and accessibility of the acid sites. The structural and textural properties of the catalysts were investigated using X-ray diffraction (XRD) and N_2 adsorption. HR-TEM was used to assess the dispersion and location of Pd nanoparticles on HPSAPO-5. The spent catalyst could be restored and reused after calcination.

© 2021 Elsevier Inc. All rights reserved.

1. Introduction

Lignocellulose is the most abundant and inexpensive source of nonedible biomass that can be used for the synthesis of fuels, chemicals and materials [1-5]. Among the different intermediates that can be produced from carbohydrates, furanic compounds hold a strategic place. In particular, furfural (FF) and 5-hydroxymethylfurfural (HMF), which can be accessed by the acid-catalyzed dehydration of pentoses and hexoses [6-8], respectively, are considered by the U.S. Department of Energy (DoE) as two of the most value-added biomass building blocks or platform chemicals [9]. Both bio-based furanic derivatives can be further oxidized, hydrolyzed or reduced to generate valuable downstream chemicals, such as methyl- and dimethylfuran or tetrahydrofuran [10], levulinic acid [86], γ-valerolactone [11], furandicarboxylic acid [12], maleic acid [13], and hydrocarbons [14-19].

Functionalizing bio-based furanic derivatives in a minimum number of synthetic steps is of huge interest to increase the molecular diversity and complexity. In this view, it would be desirable to devise simple, easily accessible and robust catalytic systems affording multi-step reactions to engineer intensified processes avoiding the separation of intermediates. Sequential [21,22,24,29] and one-pot [87,88] reactions have been developed targeting the synthesis of branched alkanes as jet fuels and monomers for polyester and epoxy resins starting from the aldol condensation reaction of FF with ketones (e.g., acetone, methyl isobutyl ketone, cyclopentanone), followed by hydrodeoxygenation (HDO) at solvent-free conditions. Likewise, one-pot reactions have also been reported for the synthesis of furan- and THF-derived alcohols and amines by the one-pot (one-reactor tandem) aldol condensation reaction of FF with ketones, followed by hydrogenation with H_2 [20,30,89,90], or reductive amination with NH_3 and H_2 [31,32], respectively.

Considerable research has been carried out in the last years to engineer basic catalysts for conducting aldol condensation reactions of FF and ketones, including metal and mixed oxides (e.g., ZrO_2, ZnO, $MgO-ZrO_2$) [33-37], zeolites [38,39] and metal-substituted zeotypes [40]. However, fewer examples have been reported on acid catalysts, relying on acid oxides (e.g., ZrO_2 and ZnO) [41], acid zeolites [42-44] and metal–organic frameworks [45]. Zeolites are particularly attractive due to their tunable acid properties, but can exhibit poor activity due to mass transport

limitations within micropores, affecting the accessibility of the reagents to the acid sites, as well as low hydrothermal stability and deactivation due to coke deposition [46-50]. To overcome these shortcomings, hierarchical acid zeolites have been developed using different methodologies, some of which have recently shown promising results in aldol condensation reactions [51,52]. In particular, hierarchical silicoaluminophosphates (SAPOs) acid zeo-type catalysts represent a viable alternative. Indeed, microporous SAPOs have been extensively used in acid catalyzed reactions for hydrocarbon conversion [53,54]. In particular, SAPO-5, with an AFI framework, a pore diameter of 7.3 Å and moderate acidity, has been used as heterogeneous catalyst in methanol-to-olefin conversion, toluene alkylation [55] and xylene isomerization [56]. Recently, hierarchical SAPO catalysts combining the micropores of the zeolite framework and an additional mesoporous network, have been synthesized using both top-down [57,58] and bottom-up strategies [59-64].

Herein, a novel bottom-up approach was used to synthesize hierarchical SAPO-5 catalysts (HPSAPO-5). This method avoids post-synthetic demetallation under acid or basic conditions as commonly found in top-down methods, resulting in a localized collapse of the zeolite framework. A series of HPSAPO-5 catalysts with variable Si loadings were prepared using cetyl trimethylammonium bromide (CTAB) encapsulated within MCM-41, serving both as Si source and mesoporogen [62]. This particular synthetic methodology mitigates the use of expensive and sophisticated surfactants to induce mesoporosity in the microporous framework, and benefits from a superior retention of the acid properties of microporous SAPOs, whilst simultaneously enhancing mass transfer. The Si loading allows a modulation of the acid density and strength by a partial substitution of framework P with Si [65], resulting in the formation of Brønsted acid sites of medium acid strength [66,67] through a type-2 substitution mechanism (SM2) [68]. An increase of the Si loading can also induce the formation of silica islands in SAPO frameworks, altering the acid strength. Besides, by impregnating Pd over HPSAPO-5, a bifunctional catalyst can be designed, affording the formation of furan- and tetrahydrofuran-derivatives in an efficient one-step process starting from FF and ketones. These products could be applied as potential biofuels or biosolvents.

2. Experimental

2.1. Materials

Aluminum isopropoxide (≥98%), triethylamine (≥99.5%), tetraethyl orthosilicate (≥99%) and phosphoric acid (85 wt% in H_2O), all used for the synthesis of SAPO-5, were supplied by Sigma-Aldrich (Milano, Italy). Palladium(II) acetate (98%), also supplied by Sigma-Aldrich, was used for the synthesis of Pd/SAPO-5 catalysts. NH_3 (≥99.7%), purchased from SIAD (Bergamo, Italy), and 2,6-di-*tert*-butylpyridine (≥97%), purchased from Sigma Aldrich (Milano, Italy), were used as probe molecules in the FTIR experiments. Furfural (99%) and methyl isobutyl ketone (≥99%), both procured form Sigma-Aldrich, were used for the catalytic tests. ZSM-5 (Si/Al = 23), ZSM-5 (Si/Al = 80), ZSM-5 (Si/Al = 200), ZSM-5 (Si/Al = 280) and Y (Si/Al = 30) were purchased from Zeolyst, while BEA (Si/Al = 150) was supplied by Clariant and MOR (Si/Al = 6.1) was kindly supplied by ITQ. ZnO and ZrO_2 were procured from Sigma-Aldrich.

2.2. Synthesis of Al-SBA-15 (Si/Al = 76)

The Al-doped SBA-15 catalyst with a nominal SiO_2/Al_2O_3 molar ratio of 76 was prepared by the evaporation-induced self-assembly (EISA) method. The preparation method can be found elsewhere [69]. Briefly, 2.0 g of Pluronic P-123 triblock co-polymer was dis-

solved in 38 mL of anhydrous ethanol. Then, 4.16 g (20 mmol) of tetraethylorthosilicate (TEOS) and 0.054 g (0.26 mmol) of aluminium isopropoxide $[(CH_3)_2CHO]_3Al$ and deionized water were added under vigorous stirring. After stirring for 24 h at room temperature, the mixture was poured into a Petri dish to initiate the EISA process. The as-obtained gels were calcined at 550 °C for 6 h under static air with a heating rate of 1 °C min^{-1}.

2.3. Synthesis of microporous SAPO-5 with variable Si loading

Aluminium isopropoxide (7.0 g) was added slowly to deionized water (10 mL) and triethylamine (TEA, 2.77 mL) under stirring, and the mixture was further stirred for 1 h. Tetraethylorthosilicate (TEOS, 2.31 mL, 4.62 mL and 6.92 mL for Si = 0.30, Si = 0.60 and Si = 0.90, respectively) was added dropwise under stirring, along with 7.29 mL of deionized water, and the mixture was further stirred for 2 h. Phosphoric acid (2.18 mL, 85 wt% in H_2O) was added dropwise under stirring. The gel was vigorously stirred for 30 min to produce a white gel with the following composition:

1 Al:0.93P:x Si:0.58 TEA:28 H_2O where x = 0.3; 0.6; 0.9.

The gel was transferred to a Teflon-lined stainless-steel autoclave and subjected to hydrothermal synthesis at 473 K for 60 h under autogenous pressure. The solid product was then recovered from the autoclave by filtration, washed with water, dried in air at 373 K and finally calcined in a tube furnace at 873 K for 16 h under airflow to generate a white crystalline solid.

For the sake of clarity, the nomenclature SAPO-5/*x*Si is hereinafter used, where 'x' refers to the molar Si content in the synthetic gels.

2.4. Synthesis of hierarchical HPSAPO-5 with variable Si loading

Aluminium isopropoxide (7.0 g) was added slowly to deionized water (10 mL) and TEA (2.77 mL) under stirring, and the mixture was further stirred for 1 h. CTAB-containing MCM-41 (1.03 g, 2.06 g and 3.09 g for Si = 0.30, Si = 0.60 and Si = 0.90, respectively) was slowly added, and the mixture was further stirred for 2 h. Phosphoric acid (2.18 mL, 85 wt% in H_2O) was added dropwise under stirring. The mixtures with three variable Si contents were vigorously stirred for 30 min to produce white gels with the following composition

1 Al: 0.93P: x Si: y CTAB:0.58 TEA: 28 H_2O where x = 0.3 and y = 0.033; x = 0.6 and y = 0.066; x = 0.9 and y = 0.099.

The gels were transferred to a Teflon-lined stainless-steel autoclave and crystallized at 473 K for 60 h under autogenous pressure. The solid product was then recovered from the autoclave by filtration and washed with water. The as-prepared product was dried in air at 373 K and calcined in a tube furnace under airflow at 873 K for 16 h to remove organic surfactant and micropore template, producing a white crystalline solid.

For the sake of clarity, the nomenclature HPSAPO-5/*x*Si is hereinafter used, where 'HP' refers to 'hierarchical porous, and 'x' refers to the molar Si content in the synthetic gels.

2.5. Synthesis of Pd/HPSAPO-5Si = 0.9

4.9 g of HPSAPO-5, 0.9Si were dispersed in a solution of 0.54 g of palladium acetate in 30 mL of acetone. The final suspension was sonicated for 30 min, and acetone was evaporated at 313 K under vigorous stirring. The sample was then dried in an oven overnight at 353 K, calcined at 673 K for 4 h and reduced at 473 K for 4 h under H_2.

2.6. Catalyst characterization

Before undertaking structural, volumetric and spectroscopic analysis, calcined samples were outgassed at 573 K to remove adsorbed water.

The phases present in the different catalysts were analyzed by powder X-ray diffraction (PXRD). The PXRD patterns were recorded on a PANalytical X'Pert PRO diffractometer provided with Cu-Kα radiation (λ = 1.54062 Å) generated at 45 kV and 30 mA. The spectra were collected in the range $5° \leq 2\theta \leq 40°$ with a step size of 0.02°. The patterns were indexed using the Joint Committee on Powder Diffraction (JCPDS) database.

The textural properties of the catalysts were inspected by N_2 and Ar physisorption at 77 K in the relative pressure range from 1×10^{-6} to 1 P/P_0 using a Quantachrome ASiQ apparatus. Prior to the analysis, the samples were outgassed at 573 K for 24 h (residual pressure lower than 10^{-6} Torr). Specific surface areas were determined by the Brunauer-Emmett-Teller (BET) method in the relative pressure range from 0.01 to 0.1 P/P_0. The adsorption branch was analyzed by the NLDFT (non-local density functional theory) method to obtain the pore size distributions of the different samples [70-72].

FTIR spectra of self-supporting pellets were collected under vacuum conditions (residual pressure < 10^{-5} mbar) using a Bruker Equinox 55 spectrometer equipped with a pyroelectric detector (DTGS type) with a resolution of 4 cm^{-1}. NH_3 and 2,6-di-*tert*-butylpyridine (2,6-dTBP) were adsorbed at room temperature using specially designed cells permanently connected to a vacuum line to perform adsorption–desorption *in situ* measurements. FTIR spectra were normalized with respect the pellet weight and, whenever specified, were reported in difference-mode by subtracting the spectrum of the sample in vacuum from the spectrum of the adsorbed molecules. The total number of accessible Brønsted acid sites (N) was estimated using the Lambert-Beer law in the form A = εNρ, where A is the integrated area of the bands of the protonated species (cm^{-1}), ε is the molar extinction coefficient (cm^2. μmol^{-1}), N is the concentration of the vibrating species (μmol g^{-1}), and ρ is the density of the disk (mass/area ratio of the pellet, mg cm^{-2}) [73].

Solid-state (SS) NMR spectra were acquired on a Bruker Avance III 500 spectrometer and a wide bore 11.7 Tesla magnet with operational frequencies for ^{1}H, ^{29}Si, ^{31}P and ^{27}Al of 500.13, 99.35, 202.45 and 130.33 MHz, respectively. A 4-mm triple resonance probe in double resonance mode with magic angle spinning (MAS) was employed in all the experiments, and the samples were packed on a Zirconia rotor and spun at a MAS rate of 15 kHz. The magnitudes of radio frequency fields were 100, 83 and 42 kHz for ^{1}H, ^{31}P and ^{29}Si respectively. The ^{27}Al MAS spectra were acquired on large sweep width with small pulse angle (π/12) to ensure quantitative interpretation. In the case of ^{29}Si, ^{31}P and ^{27}Al MAS NMR, high-power proton decoupling was applied. The relaxation delay, d1, between accumulations was 5, 1, 20, and 60 s for ^{1}H, ^{27}Al, ^{31}P and ^{29}Si MAS NMR spectra, respectively. All chemical shifts were reported using δ scale, and were externally referenced to TMS for ^{1}H and ^{29}Si NMR, Al(H$_2$O)$_6^{3+}$ ion in 1.0 m AlCl$_3$ solution for ^{27}Al NMR and H$_3$PO$_4$ (85%) for ^{31}P NMR. The chemical shifts for ^{27}Al NMR were not corrected by second-order quadrupole effects. The ^{1}H MAS NMR spectra were fitted (DMFIT) for quantitative deconvolution of overlapping peaks. The samples were packed into a NMR rotor and dehydrated at 573 K under vacuum (1×10^{-4} mbar) for 2 h prior to loading into the magnet and recording the NMR spectra.

NH$_3$-TPD was used to measure the density and strength of acid sites in the catalysts. The measurements were performed on a Micromeritics AutoChem II 2920 system equipped with a quartz U-type tubular reactor and a thermal conductivity (TCD) detector.

A typical test was carried out as follows: 70 mg of catalyst were pre-treated at 250 °C for 2 h under a He flow [40 mL(STP)/min] to remove adsorbed moisture and vapors, and then cooled down to room temperature. Subsequently, NH$_3$ was chemisorbed at 100 °C using pulsed injections until saturation. The temperature was then increased up to 1000 °C using a heating rate of 10 °C/min and the TPD profiles were recorded from 100 to 1000 °C. The quantification method used for measuring the number of acid sites can be found elsewhere [74,75]. All the profiles were normalized to a constant mass of wafer.

The H$_2$-TPR profiles were collected for Pd-containing catalysts on a Micromeritics AutoChem II2920 system equipped with a quartz U-type tubular reactor and a TCD detector. A cold trap was used before the detector to avoid any interference of water in the TPR plot. In each test, 50 mg of the given catalyst was loaded into the reactor and purged with 30 mL(STP)/min He at 300 °C for 1 h to remove adsorbed moisture and vapors, and then cooled down to room temperature. The temperature was then increased up to 750 °C at a heating rate of 10 °C/min under a H$_2$ flow diluted in Ar (10 v/v%). The system was calibrated using an Ag$_2$O standard (>99% purity) to measure the H$_2$ consumption in the TPR profiles. All the profiles were normalized to a constant mass of wafer.

Inductively Coupled Plasma Atomic Emission Spectroscopy (ICP-AES) was used to quantify the bulk Pd content of the catalysts using a Thermo IRIS Intrepid II XSP atomic emission spectrometer. Before the measurements, the samples were dissolved using a HNO$_3$/H$_2$SO$_4$/HF solution.

2.7. Catalytic tests

The aldol condensation/crotonization reaction was conducted in a stainless steel autoclave reactor (30 mL) from Taiatsu. In a typical test, the autoclave was charged with 0.2 g (2 mmol) of distilled FF, 3.8 g (38 mmol) of MIBK, and 40 mg of catalyst (optimized conditions) with a magnetic stirring bar. The mixture was heated to the desired temperature under a stirring speed of 1000 rpm, and the kinetic profiles were measured out for 1–24 h. Preliminary experiments were conducted ensuring the absence of external mass transfer limitations on the reaction rate.

The one-pot reaction was conducted by performing first the aldol condensation/crotonization reaction between FF and MIBK in an autoclave (30 mL) at the conditions described above, followed by the introduction of H$_2$ at the desired pressure (10–20 bar), and the hydrogenation reaction was conducted at 80–160 °C for 6–12 h ensuring complete reduction of the Pd phase according to the H$_2$-TPR profiles of the catalysts.

In each experiment, the FF conversion, selectivity, yield and the initial reaction rate of formation ($r_{i,0}$) of each product, as well as the carbon balance (CB), were defined using the following expressions (Eqs. (1)–(6))

$$FF \text{ conversion} = 1 - \frac{n_{FF}}{n_{FF}^\circ} \times 100 \tag{1}$$

$$Selectivity_i = \frac{n_i}{n_{FF}^\circ - n_{FF}} \times 100 \tag{2}$$

$$Yield_i = \frac{n_i}{n_{FF}^\circ} \times 100 \tag{3}$$

$$r_{i,0} = \frac{1}{W} \frac{dn_i}{dt} \Big| \tag{4}$$

$$CB_{FF} = \frac{\sum n_i + n_{FF}}{n_{FF}^\circ} \times 100 \tag{5}$$

$$CB_{FF+MIBK} = \frac{\sum n_i + n_{FF} + n_{MIBK}}{n_{FF}^{\circ} + n_{MIBK}^{\circ}} \times 100 \qquad (6)$$

where n_i is the number of moles of product i, and W is the catalyst loading.

The initial reaction rate of formation of the different products was measured from the kinetic plots using rational polynomial functions (1st order numerator, 2nd order denominator) for fitting the kinetic curves. The parameters in the rational polynomial functions were fitted using a least-square non-linear optimization method based on the Levenberg-Marquardt algorithm by comparison of predicted and experimental yields as a function of time.

After the reaction, the mixture was centrifuged to separate the solution from the catalyst. The concentration of the non-reacted FF and MIBK, as well as the reaction products, were analyzed and quantified by gas chromatography on a Thermo Scientific Trace 1100 GC equipped with a flame ionization detector (FID) and a HP-5 capillary column with 5 wt% phenyl groups (length 30 m; inner diameter 0.25 mm). The analytical methods were adjusted for the different mixtures depending on the boiling point and polarity of the compounds. In all the methods, the injector temperature was set at 250 °C, the detector temperature was 300 °C and the sample injection volume was 2 μL. The calibration was performed using biphenyl as internal standard for the aldolization products and dodecane for the hydrogenation products. Control experiments in the absence of catalyst revealed that the reaction did not proceed (<1% conversion).

Nuclear magnetic resonance spectroscopy (NMR) was used to determine the structure of organic compounds. Each compound can be characterized using several descriptors including the chemical shift, spin multiplicity, coupling constants, and integration. In this study, liquid ^1H NMR analysis was used to identify the structure of the products generated in the different reactions. The NMR spectra were recorded on a 400 MHz Bruker spectrometer.

3. Results and discussion

3.1. Aldol condensation/crotonization of FF with MIBK over acid zeolites

In a first step, we investigated the catalytic performance of a library of reference acid catalysts in the aldol condensation/crotonization reaction of FF and MIBK, including ZrO₂, ZnO and a series of acid zeolites with variable topologies, i.e. ZSM-5 (Si/Al = 23–280), BEA (Si/Al = 150), MOR (Si/Al = 6.1) and SAPO-5 with variable Si loadings (SAPO-5/xSi, x = 0.3, 0.6, 0.9). In all cases, the main product was (E)-1-(furan-2-yl)-5-methylhex-1-en-3-one (ALD-1) (Scheme 1), whereas (E)- and (Z)-3-(furan-2-ylmethylene)-4-methylpentan-2-one (ALD-2a and ALD-2b, respectively) were obtained as by-products. The alcohol intermediate issued from the aldol condensation was only observed at trace levels for a FF conversion higher than 10%. Besides, no products issued from the aldol self-condensation/crotonization of MIBK were detected. Table 1 compiles the FF conversion, ALD-1 and ALD-2a / ALD-2b selectivities and ALD-1 yield, as well as the carbon balance with respect to FF, for the different catalysts.

ZnO and ZrO₂ (entries 1 and 2) display only 18% and 25% FF conversion, respectively, with an ALD-1 selectivity of 76% and 32%. Regardless of the Si/Al molar ratio, the ZSM-5 zeolites (channel size = 5.5 Å) exhibit poor FF conversion (range 10–20%) and an ALD-1 selectivity up to 60% for ZSM-5 (Si/Al = 80) (entries 3–6). Similar results are obtained for BEA (channel size = 5.5 Å) and MOR (channel size = 6.7 Å) (entries 7 and 8). In contrast, Y zeolite (cavity size = 7.4 Å) displays a higher FF conversion (40%) and 52% selectivity to ALD-1 (entry 9). The microporous SAPO-5/xSi zeolites with a comparable micropore size (7.3 Å), show similar FF conversion,

especially for x = 0.6 and x = 0.9, with values of 49% and 40% (entries 12 and 14), respectively, while the FF conversion for SAPO-5/0.3Si is only 23% (entry 10). In parallel, the ALD-1 selectivity is about 60% for SAPO/0.6Si and SAPO-5/0.9Si, approaching the value obtained for ZSM-5 (Si/Al = 80) and Y zeolites, whereas SAPO-5/0.3Si shows a much lower ALD-1 selectivity of 47%. The selectivity of the aldolization by-products ALD-2a and ALD 2b is similar for the different SAPO-5/xSi samples with a value in the range 8–10%.

We further investigated the catalytic activity of the hierarchical HPSAPO-5/xSi zeolites (x = 0.3, 0.6, 0.9). A neat increase of the FF conversion is observed for HPSAPO-5/0.9Si (entry 15) and HPSAPO-5/0.3Si (entry 11) compared to the parent SAPO-5/0.9Si (73% *vs.* 49%) and SAPO-5/0.3Si (45% *vs.* 23%), respectively, whereas no apparent change is observed for HPSAPO-5/0.6Si (49%, entry 13). The ALD-1 selectivity for HPSAPO-5/0.9Si and HPSAPO-5/0.6Si is comparable to that obtained for the parent zeolites, but the selectivity is much higher for HPSAPO-5/0.3Si compared to SAPO-5/0.3Si (72% *vs.* 47%). The selectivity of the aldolization by-products ALD-2a and ALD-2b is similar for the different HPSAPO-5/xSi samples with a value about 13%, which is slightly higher than the value obtained on the parent SAPO-5/xSi samples. To assess for the role of mesoporosity on the catalytic properties, we measured the catalytic activity for Al-SBA-15 (Si/Al = 76) (entry 16). Unlike the HPSAPO/xSi catalysts, especially HPSAPO/0.9Si, the FF conversion and ALD-1 selectivity are lower, with values in line to those obtained for Y zeolite.

Overall, the results presented above point out an important effect of the Si loading and the presence of a hierarchical architecture on the catalytic properties of acid SAPO-5 catalysts in the aldol condensation/crotonization reaction of FF with MIBK. The acid properties and pore architecture of HPSAPO-5/xSi make these catalysts attractive for the reaction unlike microporous zeolites and other reference acid catalysts. These encouraging results prompted us to study in detail the reaction kinetics of the HPSAPO-5/xSi at different temperatures.

3.2. Kinetic profiles for FF + MIBK aldolization/crotonization over HPSAPO-5/xSi

The kinetic profiles were measured for the HPSAPO-5/xSi and the parent SAPO-5/xSi catalysts in the temperature range 140–180 °C. The initial FF:MIBK molar ratio was set to 1:18 (5.2 wt% FF) while keeping the FF-to-catalyst weight ratio at a constant value of 5.0 to promote the formation of ALD-1 and keep a high carbon balance with respect to FF (see SI, Fig. S1). Fig. 1 plots the curves obtained for the FF conversion and the ALD-1 and ALD-2a, b selectivites, whereas Fig. 2 plots the corresponding selectivity-conversion curves. Additional kinetic curves at lower temperature (120 °C) can be found in the SI (Fig. S2).

Regardless of the temperature, HPSAPO-5/0.3Si exhibits a monotonous increase of the FF conversion with the reaction time until a plateau value lower than 100%, which increases with the temperature from *ca.* 30% at 140 °C (Fig. 1C1) to 60% at 180 °C (Fig. 1C3) after 24 h. An analogous trend is observed for the parent SAPO-5/0.3Si, with an almost complete superposition of the kinetic curves at longer reaction times for the different temperatures, although a markedly lower conversion is observed for times below 12 h. The presence of a plateau in the FF conversion can be explained by a potential catalyst deactivation during the reaction, which appears to be unaffected by the porous texture of the catalysts. As a matter of fact, the carbon balance with respect to FF decreases along the reaction with a final down to 80% (see SI, Fig. S3). However, the total carbon balance (including MIBK) keeps at a value higher than 95%.

Unlike HPSAPO-5/0.3Si, HPSAPO-5/0.6Si and HPSAPO-5/0.9Si do not display a plateau for the FF conversion at longer reaction times,
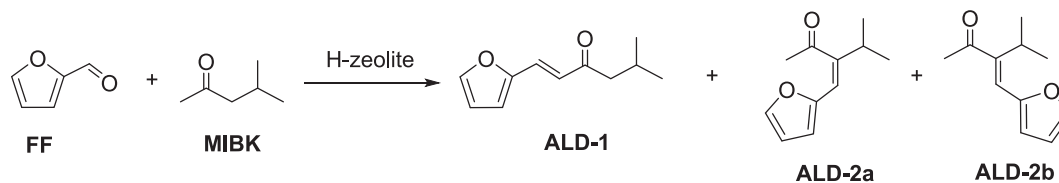
Scheme 1. Main products obtained in the aldol condensation/crotonization reaction of FF with MIBK over acid zeolites.

Table 1
Summary of catalytic properties for the different zeolites tested in this study.[*]

Entry	Catalyst	Conv FF (%)	Sel ALD-1 (%)	Sel by-products (%)	Yield ALD-1 (%)	CB$_{FF}$ (%)
1	ZnO	25	76	14	19	87
2	ZrO$_2$	18	32	5	6	83
3	ZSM-5 (Si/Al = 23)	14	25	5	4	80
4	ZSM-5 (Si/Al = 80)	20	60	6	12	83
5	ZSM-5 (Si/Al = 200)	10	46	4	5	85
6	ZSM-5 (Si/Al = 280)	13	28	6	4	82
7	BEA (Si/Al = 150)	26	42	4	11	80
8	MOR (Si/Al = 6.1)	16	64	4	10	82
9	Y (Si/Al = 30)	40	52	5	20	84
10	SAPO-5/0.3Si	23	47	9	11	83
11	HPSAPO-5/0.3Si	45	72	13	32	81
12	SAPO-5/0.6Si	49	57	10	28	79
13	HPSAPO-5/0.6Si	49	61	13	30	81
14	SAPO-5/0.9Si	40	60	8	24	87
15	HPSAPO-5/0.9Si	73	62	14	46	76
16	Al-SBA-15 (Si/Al = 76)	38	45	7	17	84

[*] Reaction conditions: 0.2 g FF, 3.8 MIBK, 40 mg catalyst, 180 °C, 3 h.

even if the reaction proceeds slowly in the former case after 12 h, and reach higher FF conversions. The FF conversion evolves from 56% at 140 °C (Fig. 1B1) to 65% at 180 °C (Fig. 1B3) for HPSAPO-5/0.6Si, and from 60% at 140 °C (Fig. 1A1) to full conversion at 180 °C (Fig. 1A3) for HPSAPO-5/0.9Si, after 24 h. These results suggest that, whereas both samples show partial deactivation during the reaction, this is much less prominent on HPSAPO-5/0.9Si.

A similar conclusion can be drawn from the kinetic plots on the parent SAPO-5/0.6Si and SAPO-5/0.9Si, but with two divergent behaviors compared to the hierarchical counterparts: SAPO-5/0.6Si exhibits higher FF conversions compared to HPSAPO-5/0.6Si, especially at 160 °C, with a FF conversion reaching 75% after 24 h, whereas SAPO-5/0.9Si exhibits much lower FF conversions compared to HPSAPO-5/0.9Si, even at the highest temperature (180 °C) and long reaction times. This different behavior points out a positive effect of the hierarchical architecture on the catalytic activity for HPSAPO-5/0.9Si, whereas the effect is low and even detrimental for HPSAPO-5/0.6Si.

Turning now our attention into the selectivity, irrespective of the temperature, the microporous SAPO-5/xSi catalysts exhibit a sharp increasing trend for the ALD-1 selectivity until a plateau value at about 60%, especially for SAPO-5/0.3Si. This becomes clearly visible in the selectivity-conversion plots, especially at lower temperature (140 °C) (Fig. 2A2–C2). In contrast, the hierarchical HPSAPO-5/xSi catalysts show a less prominent increase of the ALD-1 selectivity with the FF (Fig. 2A1–C1), being almost constant for HPSAPO-5/0.9Si. In all cases, the aldol by-products ALD-2a and ALD-2b show similar selectivities for the hierarchical and parent SAPO-5 catalysts with a selectivity up to 15% at 180 °C after 24 h.

The increasing trend of the ALD-1 selectivity for SAPO-5/xSi suggests a hindering effect of internal mass transfer on the reaction rate due to a poor accessibility of FF and MIBK to the acid centers in the zeolite micropores. This accessibility is promoted at higher temperature, enhancing the diffusivity of the reactants and ALD-1 within the micropores. In the case of hierarchical HPSAPO-5/xSi

catalysts, the presence of mesopores enriched with Si-OH groups on the external surface is expected to favor mass transfer between SAPO-5 particles and promote MIBK adsorption (*vide infra*), enhancing the reaction at lower FF conversion. Besides, the presence of a plateau for the ALD-1 selectivity (<100%) at high FF conversion can be attributed to catalyst deactivation, blocking the accessibility to the acid centers in the micropores.

3.3. Reaction rates, reaction order and activation energies for ALD-1 synthesis

The initial reaction rates of ALD-1 formation were measured from the time-evolution of the ALD-1 yield (see SI, Figs. S4, S5) using Eq (4) and rational polynomial functions for fitting the kinetic curves. The parity plots are collected in Fig. S6. Fig. 3 plots the rates on HPSAPO-5/xSi and SAPO-5/xSi as a function of the temperature and the Si loading (x). Among the SAPO-5/xSi catalysts (Fig. 3B), the initial rate of ALD-1 formation is sensibly higher on SAPO-5/0.6Si, especially at 140 °C, evolving from 2.6 mmol.g^{-1}.h^{-1} at 140 °C to 12 mmol.g^{-1}.h^{-1} at 180 °C. In contrast, among the HPSAPO-5/xSi catalysts (Fig. 3A), the highest rates are observed on HPSAPO-5/0.9Si for all temperatures, reaching a value as high as 110 mmol.g^{-1}.h^{-1} at 180 °C. When comparing the initial reaction rates of ALD-1 formation on HPSAPO-5/xSi and SAPO-5/xSi catalysts (Table 2), the highest enhancement is observed for HPSAPO-5/0.9Si with ratios of 30, 16 and 17 at 140 °C, 160 °C and 180 °C, respectively. This observation points out a remarkable effect of the hierarchical architecture on the reaction rate of ALD-1 formation. In contrast, these ratios are much lower for HPSAPO-5/0.3Si (range 5.6–9.8), and especially for HPSAPO-5/0.6Si, showing ratios lower than 2 and accordingly an almost negligible effect of the hierarchical architecture on the catalytic properties.

With these results in hand, we measured the activation energies of ALD-1 formation by representing the Arrhenius plots for the HPSAPO-5/xSi and SAPO-5/xSi catalysts (Fig. 4). Within the limits of the experimental error, all the catalysts except SAPO-5/0.3Si,
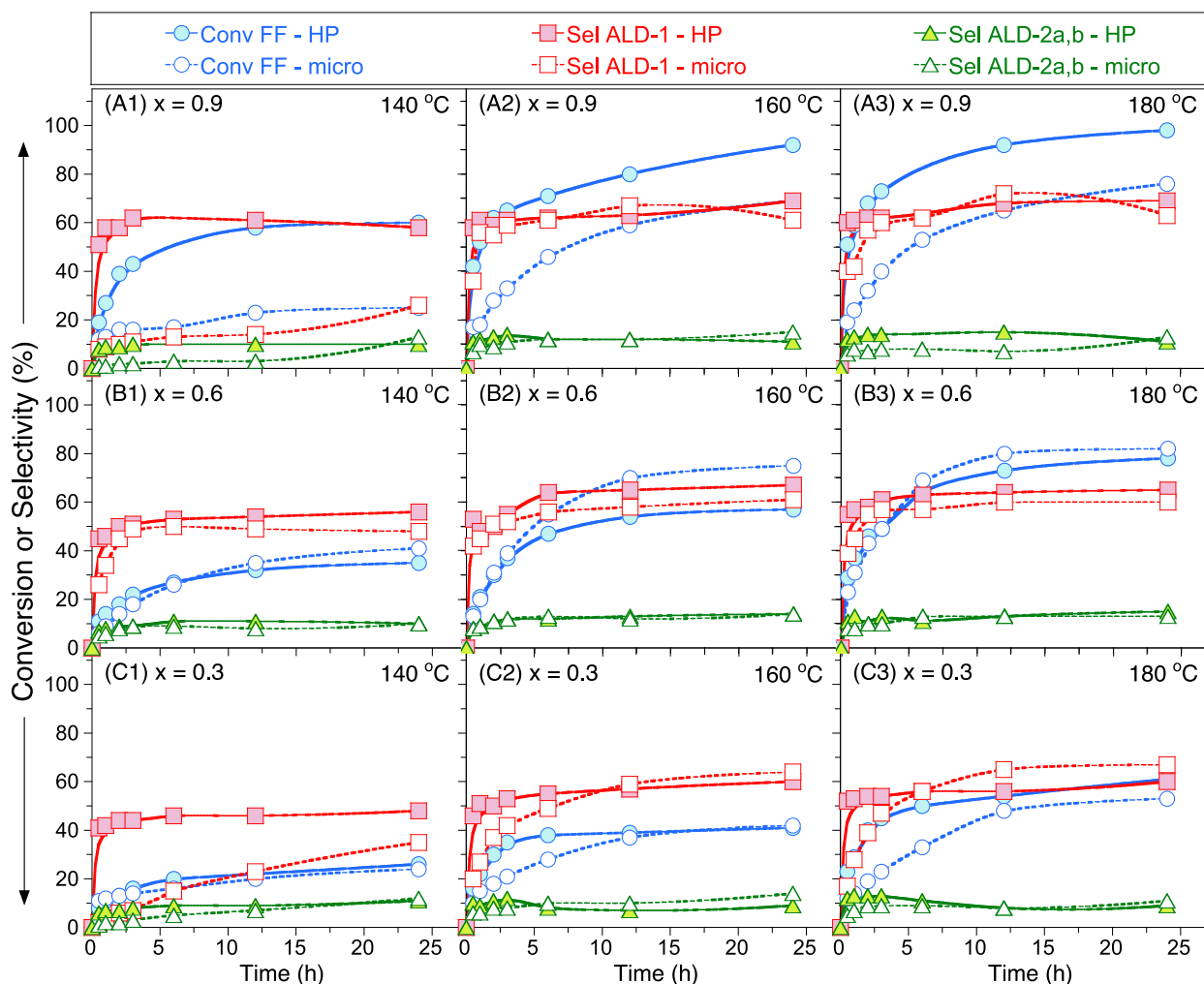
Fig. 1. Time-evolution of the FF conversion, ALD-1 and ALD-2a,b selectivity in the aldol condensation/crotonization reaction of FF with MIBK over HPSAPO-5/xSi (filled symbols, straight lines) and SAPO-5/xSi (empty symbols, dotted lines) at different temperature: (A) x = 0.9, (B) x = 0.6 and (C) x = 0.3. Reaction conditions: 0.2 g FF, 3.8 g MIBK, 40 mg catalyst, 3 h, (A1-C1) 140 °C, (A2-C2), 160 °C and (A3-C3) 180 °C.

irrespective of their porous architecture, exhibit comparable apparent activation energies at about 100 kJ/mol. This observation points out an identical catalytic mechanism for the different samples with the absence of internal mass transfer effects on the measured reaction rates. In this view, the higher activity observed on HPSAPO-5/0.9Si should be attributed, at first sight, to a higher density of accessible acid sites with the right strength (see chapter 3.6).

3.4. Catalyst recyclability and reuse

The catalyst recyclability and reuse was assessed for HPSAPO-5/0.9Si in four consecutive catalytic runs for the aldol condensation/crotonization reaction of FF with MIBK at 160 °C for 3 h (see SI, Fig. S7). The first run results in a FF conversion of 65% and ALD-1 and ALD-2a,b selectivities of 61% and 13%, respectively. After the reaction, the catalyst was separated, washed with ethanol and reused for a further catalytic test. The FF conversion decreases to 36%, whereas the ALD-1 selectivity increases to 72% at the expense of the ALD-2a,b selectivity with a value of 8%. A slight decline of the FF conversion together with an increase of the ALD-1 selectivity is observed between the 2nd-4th runs. These results reinforce the idea pointed out above of partial catalyst deactivation during the reaction, most likely by the formation of oligomers or coke in the micropores. In this view, after the fourth

run, the catalyst was separated, calcined at 400 °C under airflow and reused again. The catalytic activity is recovered, with a FF conversion of 58% and ALD-1 and AlD-2a,b selectivities of 58% and 8%, respectively.

3.5. Single-reactor tandem aldol condensation/crotonization of FF with MIBK, followed by hydrogenation

Given the high catalytic activity obtained over HPSAPO-5/0.9Si, we further investigated the single-reactor tandem aldol condensation/crotonization reaction of FF with MIBK, followed by hydrogenation (Scheme 2). To this aim, we impregnated HSAPO-5/0.9Si with Pd at three different loadings (0.3 wt%, 0.8 wt%, 4.8 wt%). First, we conducted the aldol condensation/crotonization reaction over 0.3%Pd/HSAPO-5/0.9Si and 4.8%Pd/HSAPO-5/0.9Si in the temperature range 140–180 °C. Fig. 5 plots the kinetic profiles obtained for the FF conversion and selectivity of ALD-1 and ALD-2a,b by-products. For comparison, the kinetic profiles for the parent HPSAPO-5/0.9Si are also represented. Unlike HPSAPO-5/0.9Si, 0.3%Pd/HSAPO-5/0.9Si and 4.8%Pd/HSAPO-5/0.9Si exhibit a sustained increase of the FF conversion until 100% after 12 h. The ALD-1 selectivity also exhibits a plateau, but at a higher value than in the case of HPSAPO-5/0.9Si (75% vs. 62%). The initial reaction rate of ALD-1 formation is lower in the case of 0.3%Pd/HSAPO-5/0.9Si and 4.8%Pd/HSAPO-5/0.9Si (9 mmol.g^{-1}.h^{-1} at 160 °C),
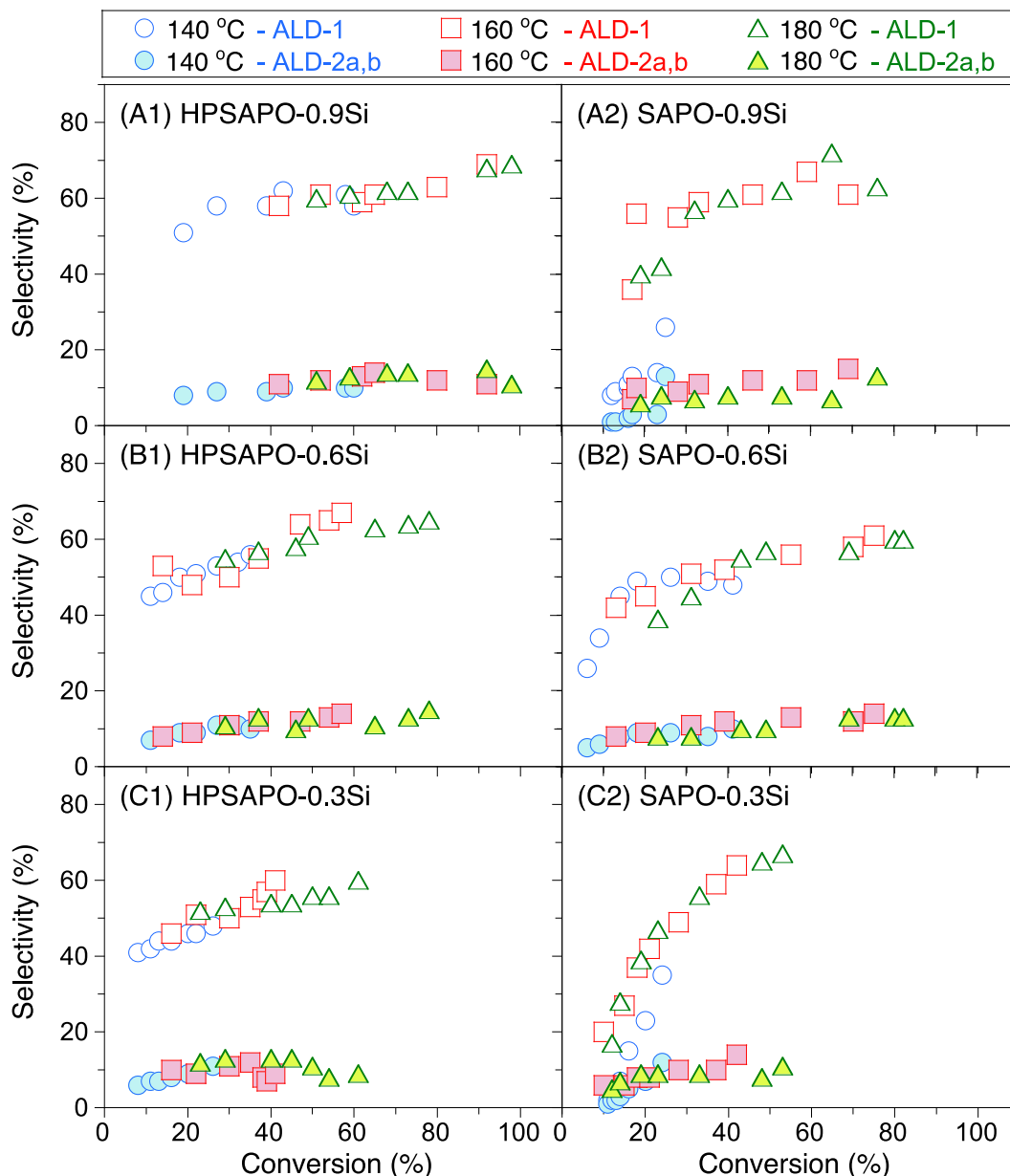
Fig. 2. Selectivity-conversion plots in the aldol condensation/crotonization reaction of FF with MIBK over (A1-C1) HPSAPO-5/xSi and (A2-C2) SAPO-5/xSi: (A) x = 0.9, (B) x = 0.6 and (C) x = 0.3. Reaction conditions as in Fig. 1.

whereas the rate measured on HSAPO-5/0.9Si is 60 mmol.g^{-1}.h^{-1} (see fittings in SI, Figs. S8, S9).

With these results in hand, we performed the single-reactor tandem aldol condensation/crotonization reaction of FF with MIBK, followed by hydrogenation, over the Pd-loaded HPSAPO-5/0.9Si catalysts. Two reaction products were obtained, that is the furan-derivative issued from the hydrogenation of the conjugated C=C bond (F-ALD-1), and the THF-derivative issued also from the hydrogenation of the furan ring (THF-ALD-1). However, the relative selectivity to both products, as well as the total yield, depends on the hydrogenation conditions (Table 3). Noteworthy, neither furan-nor THF-derivatives issued from the hydrogenation of the C=O bond are detected. The best result is obtained over 4.8%Pd/HSAPO-5/0.9Si, affording the synthesis of THF-ALD-1 with 45% yield with respect to FF. F-ALD-1 is also obtained with 5% yield. Additional hydrogenated products, including products issued from ALD-2a,b, are obtained with an overall yield of 14%.

3.6. Understanding the structure and acid properties of HPSAPO-5/xSi catalysts

The catalytic results presented above point out an enhanced activity and selectivity of HPSAPO-5/0.9Si in the aldol condensation/crotonization reaction of FF with MIBK, as well as the high efficiency of 4.8%Pd/HPSAPO-5/0.9Si for the synthesis of THF-ALD-1. In light of these results, we explored the framework structure, porous architecture, acidity and acid strength of this catalyst compared to HPSAPO-5/0.6Si and HPSAPO-5/0.3Si, as well as their microporous counterparts. We also characterized the nature of the Pd phase over HPSAPO-5/0.9Si.

3.6.1. Structural and textural properties of HPSAPO-5/xSi catalysts

The XRD patterns of HPSAPO-5/xSi and the microporous SAPO-5/xSi counterparts reveal the typical reflections belonging to the AFI framework (Fig. S10). This suggests a high phase purity and

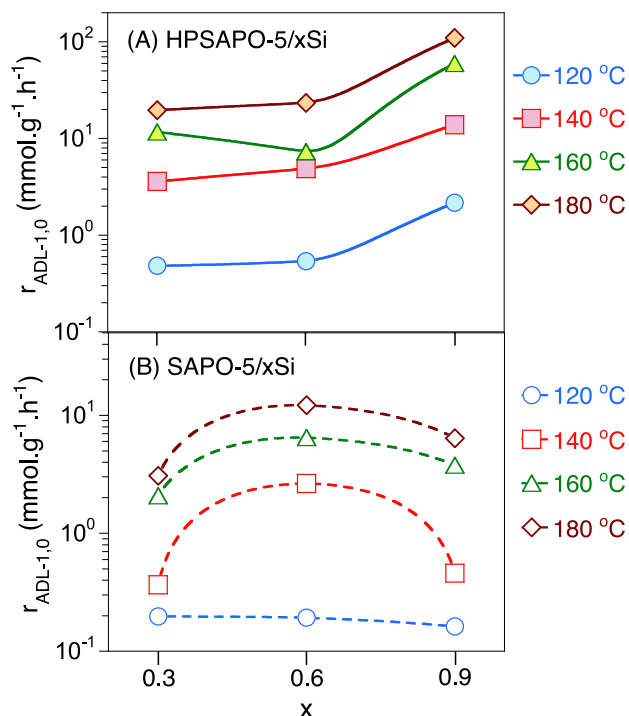**Fig. 3.** Evolution of the initial reaction rate of ALD-1 formation as a function of the temperature and the Si loading in the aldol condensation/crotonization reaction of FF with MIBK over (A) HPSAPO-5/xSi and (B) SAPO-5/xSi, with x = 0.3, 0.6, 0.9. Reaction conditions as in Fig. 1. The curves are a guide to the eye.
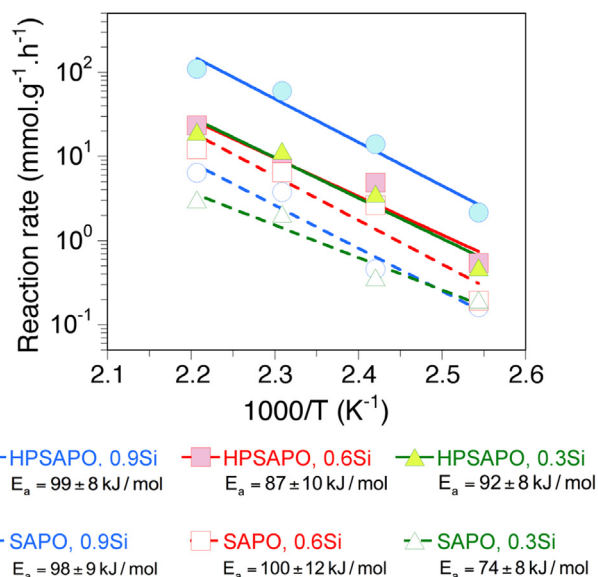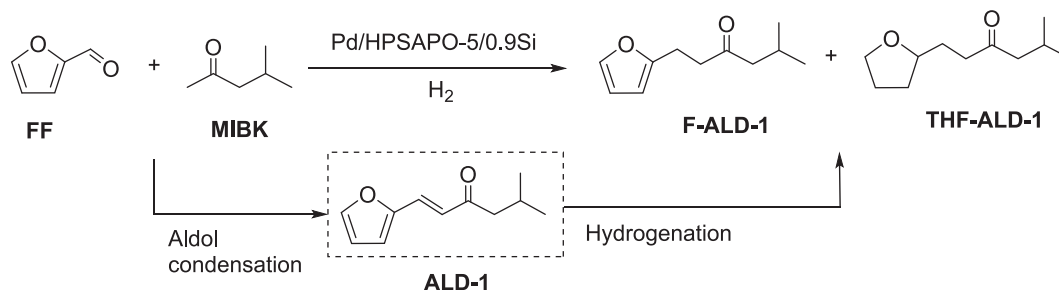

Fig. 4. Arrhenius plots for the reaction rate of ALD-1 formation in the aldol condensation/ crotonization reaction of FF with MIBK over HPSAPO-5/xSi (filled symbols) and SAPO-5/xSi (empty symbol), with x = 0.3, 0.6, 0.9. Reaction conditions as in Fig. 1.

crystallinity of all the samples regardless of their Si loading and porous architecture, both for the fresh and spent catalyst after reaction.

The presence of the hierarchical architectures, with micro- and mesoporosity, in the HPSAPO-5/xSi catalysts was evidenced by N_2 adsorption/desorption analysis at 77 K (Fig. S11A). All the hierarchical catalysts exhibit Type IV isotherms with a hysteresis loop in the P/P_0 range 0.7–1.0, which is indicative of the presence of mesopores with an average size of ca. 30 Å as inferred using the NLDFT method (Fig. S11B). Besides, a peak centered at ca. 10 Å can be visualized, which is typical of tensile strength effect due to N_2 adsorption [76]. The green distribution in panel Fig. S11B was obtained from the Ar adsorption/desorption isotherm at 77 K on HP SAPO-5/0.6Si to highlight the microporous range typical of SAPO-5, revealing a micropore size at around 7.3 Å as expected for the AFI structure.

Table 4 lists the BET surface area, as well as the total, microporous and mesoporous specific surface areas and pore volumes measured by the NLDFT method. Both the BET and NLDFT surface areas increase with the Si loading. The mesoporous surface area (S_{meso}) and mesopore volume (V_{meso}), together with total pore volume (V_{tot}), also increase with the Si loadings, while the contribution of the microporous surface area (S_{micro}) and the micropore volume (V_{micro}) are very similar in all samples. Volumetric data strongly supports the successful preparation of hierarchical architectures, and indicates the coexistence of multiple levels of porosity within HPSAPO-5.

3.6.2. Chemical environment of HPSAPO-5/xSi catalysts

The chemical environment of the framework atoms in the HPSAPO-5/xSi and the microporous SAPO-5/xSi catalysts was probed by ^{27}Al, ^{31}P, and ^{29}Si MAS NMR (Figs. S12–S14). In all cases, a unique resonance band at ca. 37 ppm is observed in the ^{27}Al NMR spectra (Fig. S12), which can be unambiguously ascribed to tetrahedrally-coordinated Al atoms in $Al(OP)_4$. This observation suggests in turn the absence of Lewis acid sites in all the catalysts. A single band at about -30 ppm is also observed in the ^{31}P NMR spectra (Fig. S13), which can be assigned to tetrahedrally-coordinated P atoms. Since both the ^{27}Al and ^{31}P NMR spectra exhibit a single resonance, it is possible to confirm a strict alternation of Al and P at the T-positions of the aluminophosphate framework [77]. In the case of the samples with the highest Si loading (i.e. x = 0.9), the ^{31}P NMR spectra exhibit a broad foot beneath the main band at ca. -24 ppm that can be assigned to P-OH units. Finally, the ^{29}Si MAS NMR spectra reveal multiple signals in the range -90 to -110 ppm due to tetrahedrally-coordinated framework Si atoms bonded to four, three, two, one and zero Al atoms (Fig. S14).

3.6.3. Acidity and acid strength of HPSAPO-5/xSi catalysts

3.6.3.1. ^1H MAS NMR. ^1H MAS NMR is an ideal tool to investigate the nature and strength of the acid sites present in SAPO-5/xSi and HPSAPO-5/xSi catalysts with different Si loadings and complements the studies performed with FTIR spectroscopy of adsorbed probe molecules (see below). ^1H MAS NMR spectra render direct information on the nature and density of protonic species present in the samples (Fig. 6, Table 5). In all cases, two well separated bands centered at around 3.5 and 4.6 ppm are visible in the spectra, which can be ascribed to two different Al(OH)Si Brønsted acid

Table 2

Ratio between the initial reaction rate of ALD-1 formation on HPSAPO-5/xSi and on SAPO-5/xSi as a function of the temperature and the Si loading (x).

x	T (°C)			
	120	140	160	180
0.30	2.4	9.8	5.6	6.4
0.60	2.8	1.8	1.1	1.9
0.90	13	30	16	17

Scheme 2. Main products obtained in the single-reactor tandem aldol condensation/crotonization reaction of FF with MIBK, followed by hydrogenation.

sites (BAS1 and BAS2) located in the 12- and 6-membered ring channels inside the AFI framework, respectively [77]. The intensity of both bands decreases with the Si loading for HPSAPO-5/xSi catalysts, while no definite trend is observed for their microporous counterparts. Whereas the intensity of both bands is similar for HPSAPO-5/0.6Si and SAPO-5/0.6Si, and for HPSAPO-5/0.3Si and SAPO-5/0.3Si, HPSAPO-5/0.9Si exhibits much lower intensity for both species compared to SAPO-5/0.9Si (21 *vs.* 12 for the species at 3.5 ppm, and 14 *vs.* 5 for the species at 4.6 ppm).

Apart from Brønsted acid sites, a signal at *ca.* 1.7 ppm is visible in all ^1H MAS NMR spectra, which can be attributed to isolated Si-OH groups, together with a band centered at around 2.6 ppm due to Al-OH and/or P-OH defects with very weak acidity [78-80]. The

intensity of the former band exhibits a neat increase with the Si loading for HPSAPO-5/xSi catalysts from 4 (x = 0.3) to 19 (x = 0.9), whereas the increase is more moderate for SAPO-5/xSi catalysts (from 11 for x = 0.3 to 15 for x = 0.9). When comparing the SAPO-5/xSi and HPSAPO-5/xSi catalysts at the same Si loading, the intensity is similar for x = 0.6 and x = 0.9, while a much lower intensity is observed for HPSAPO-5/0.3Si compared to SAPO-5/0.3Si (11 *vs.* 4). In contrast, the latter bands are systematically enhanced for HPSAPO-5/xSi catalysts compared to the SAPO-5/xSi counterparts (20 *vs.* 15 for x = 0.3, 27 *vs.* 19 for x = 0.6 and 33 *vs.* 12 for x = 0.9). Besides, for HPSAPO-5/xSi catalysts, the intensity increases monotonously with the Si loading from 20 for x = 0.3 to 33 for x = 0.9. Overall, all these results point out that, by increasing the Si loading, more defects such as Si-OH, Al-OH and/or P-OH are produced in HPSAPO-5/xSi catalysts at the expense of Brønsted acid sites.
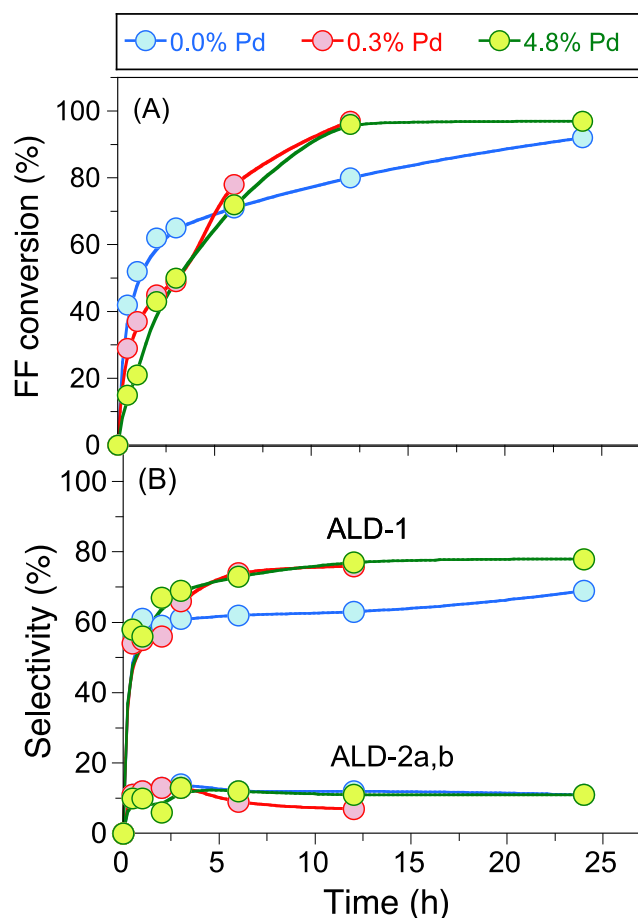
3.6.3.2. In situ vibrational FTIR spectroscopy using NH₃ and 2,6-dTBP as basic probes. The FTIR signature of O-H species in SAPO-5/xSi catalysts was reported in a previous study [54]. Briefly, the FTIR spectra are constituted by two main bands, one at 3680 cm^{-1} that can be assigned to the O-H stretching mode of free P-OH defects, and a pronounced band at 3745 cm^{-1} that can be attributed to Si-OH groups, pointing out the presence of defects in the AFI framework upon incorporation of Si.

The FTIR spectra in the OH stretching region of HPSAPO-5/xSi display two distinctive bands centered at 3630 and 3513 cm^{-1} (Fig. S15A), which can be associated to Al(OH)Si Brønsted acid sites located in the 12-ring and 6-ring channels of the AFI framework [54,78-80]. Additional signals arising from isolated SiOH (3745 cm^{-1}) and isolated POH (3678 cm^{-1}) sites are also visible, pointing out the presence of defects in the AFI framework upon incorporation of Si. In the FTIR spectra of microporous SAPO-5 (Fig. S15B), the bands due to the stretching of BAS are not visible due to the high scattering profile of the microporous SAPO-5 and only the contribution of SiOH (3745 cm^{-1}) can be appreciated [54].

The nature and accessibility of Brønsted acid sites in the HPSAPO-5/xSi catalysts can be elucidated using basic probe molecules with variable steric hindrance, such as NH₃ and 2,6-di-*tert*-butyl-pyridine (2,6-dTBP), adsorbed at room temperature. The total amount of Brønsted acid sites was measured using NH₃, which, due to its small kinetic diameter (0.26 nm), is usually considered as a suitable probe molecule for titrating acid hydroxyl groups accessible through pores, channels or windows in zeolites with a size < 4 Å [81]. In contrast, 2,6-di-*tert*-butyl-pyridine (2,6-dTBP), with a kinetic diameter of 1.05 nm, is not expected to enter the micropores, and can therefore only probe the more accessible acid sites sitting on the mesopores or in the pore mouth of micropores [82].

Fig. 7 plots the differential FTIR spectra of NH₃ and 2,6-dTBP adsorbed on HPSAPO-5/xSi catalysts in the low frequency zone, where the signals of protonated species are observed. For

Fig. 5. Time-evolution of (A) FF conversion, and (B) ALD-1 and ALD-2a,b selectivity at 160 °C in the aldol condensation/crotonization reaction of FF with MIBK over HPSAPO-5/0.9Si, 0.3%Pd/HPSAPO-5/0.9Si and 4.8%Pd/HPSAPO-5/0.9Si. Reaction conditions as in Fig. 1. The curves are a guide to the eye.

Table 3

Main products obtained in the single-reactor tandem aldol condensation/crotonization reaction of FF with MIBK, followed by hydrogenation, over Pd-loaded HPSAPO-5/xSi.

Reaction conditions		Pd (wt%)	Yield F-ALD-1	Yield THF-ALD-1	Yield Other products
1st step [*]	2nd step				
160 °C, 12 h	160 °C, 12 h, 20 bar H_2	0.3%	22%	11%	18%
		0.8%	9%	26%	13%
		4.8%	11%	22%	15%
180 °C, 3 h	160 °C, 12 h, 20 bar H_2	0.3%	12%	40%	11%
		4.8%	5%	45%	14%
180 °C, 3 h	120 °C, 3 h, 20 bar H_2	0.3%	7%	42%	14%
180 °C, 3 h	80 °C, 3 h, 20 bar H_2	4.8%	12%	8%	20%

[*] Other reaction conditions: 0.2 g FF, 3.8 MIBK, 40 mg catalyst

Table 4

Textural properties of HPSAPO-5/xSi catalysts with variable Si loading.

x	Specific surface areas (m².g⁻¹)				Pore volumes (cm³.g⁻¹)		
	SSA_{BET}	SSA_{NLDFT}	S_{micro} [†]	S_{meso} [*]	$V_{tot\ NLDFT}$	V_{micro} [†]	V_{meso}
0.30	267	375	315	60	0.304	0.079	0.225
0.60	340	450	327	123	0.323	0.077	0.246
0.90	464	552	333	219	0.448	0.075	0.373

[*] $S_{meso} = S_{DFT} - S_{micro}$.
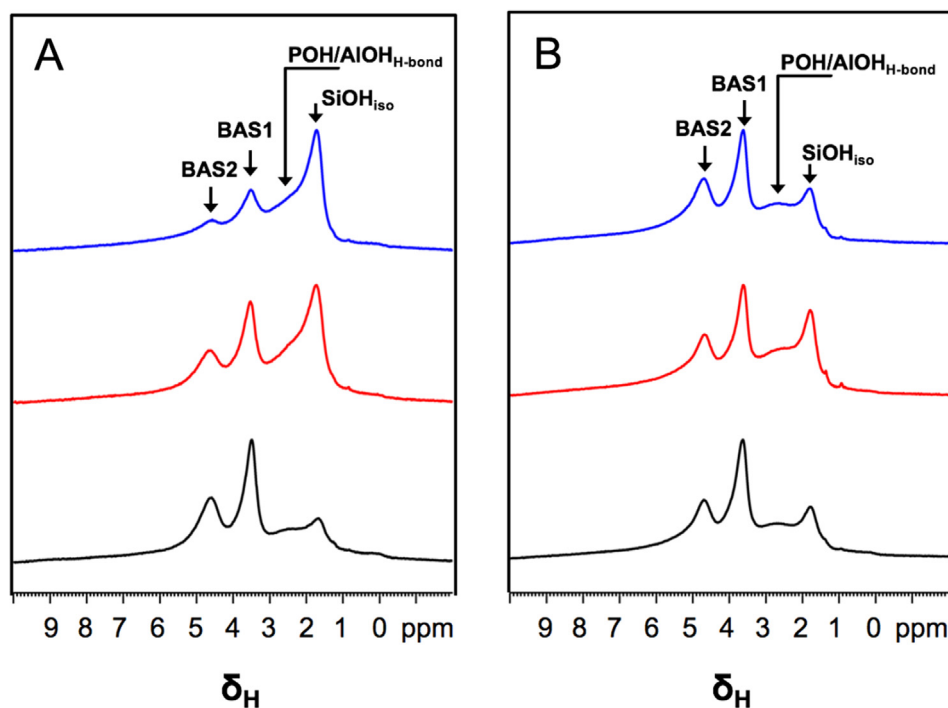
Fig. 6. ¹H MAS NMR spectra of (A) HPSAPO-5/xSi and (B) microporous SAPO-5/xSi with x = 0.30 (black curvess), x = 0.6 (red curves) and x = 0.9 (blue curves). (For interpretation of the references to color in this figure legend, the reader is referred to the web version of this article.)

Table 5

Intensity of protonic species measured from single-pulse ¹H MAS NMR spectroscopy in HPSAPO-5/xSi and microporous SAPO-5/xSi, with x = 0.3, 0.6, 0.9.

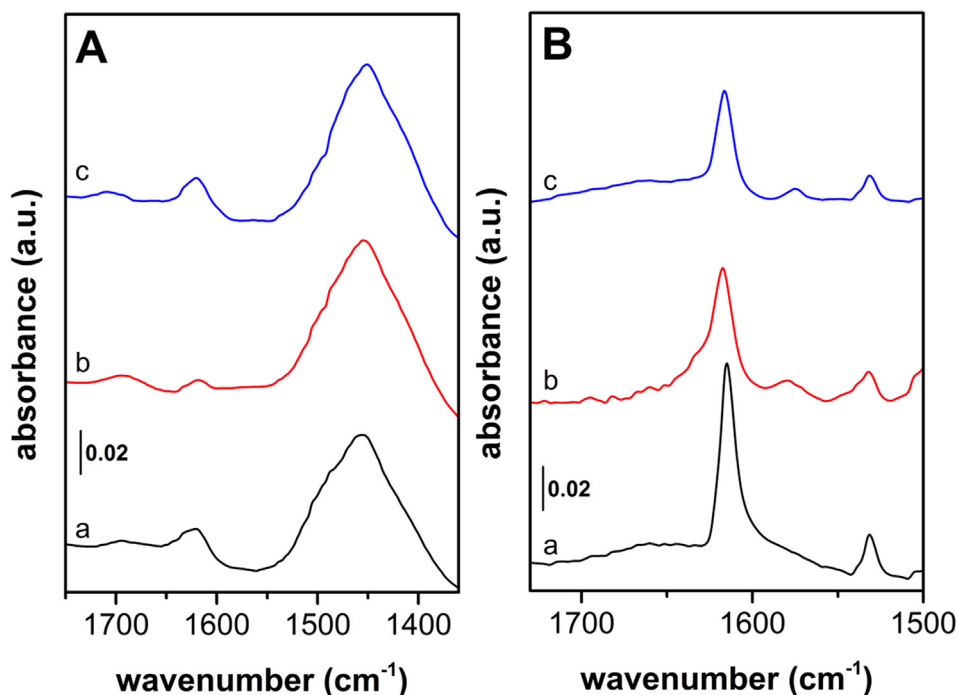| ¹H Chemical shift δ (ppm)	Assignment	HPSAPO-5/xSi			Micro SAPO-5/xSi		
		x = 0.3	x = 0.6	x = 0.9	x = 0.3	x = 0.6	x = 0.9
1.7–2.1	$SiOH_{iso}$	4	16	19	11	16	15
2.2–2.4	AlOH, POH H-bonded	20	27	33	15	19	12
3.5–3.9	BAS1	22	16	12	24	17	21
4.6–4.9	BAS2	19	11	5	13	9	14

Fig. 7. Differential FTIR spectra of (A) NH_3 and (B) 2,6-dTBP adsorption on calcined HPSAPO-5/xSi with x = 0.3 (black curves), x = 0.6 (red curves) and x = 0.9 (blue curves) after outgassing the probe molecules at room temperature. (For interpretation of the references to color in this figure legend, the reader is referred to the web version of this article.)

comparison, NH_3 was also probed on microporous SAPO-5/xSi to compare the amount of Brønsted acid sites in microporous and hierarchical catalysts (Table 6, Fig. S16). NH_3 adsorption induces proton transfer from the Brønsted acid sites to NH_3, resulting in the formation of NH_4^+ species that can be visualized in the band appearing at 1450 cm^{-1} (bending mode) (Fig. 7A). The density of accessible Brønsted acid sites (N) titrated by NH_3 is similar for microporous SAPO-5/0.3Si (46.80 $\mu mol.g^{-1}$) and SAPO-5/0.6Si (44.08 $\mu mol.g^{-1}$), whereas it shows a higher value for SAPO-5/0.9Si (52.30 $\mu mol.g^{-1}$) (Table S1). This observation points out a higher degree of Si incorporation in the SAPO-5 framework at the highest Si loading (x = 0.9). In the case of hierarchical HPSAPO-5/xSi catalysts, HPSAPO-5/0.6Si and HPSAPO-5/0.9Si contain a higher density of Brønsted acid sites with 46.25 and 45.32 $\mu mol.g^{-1}$, respectively, compared to HPSAPO-5/0.3Si, with 42.79 $\mu mol.g^{-1}$. However, HPSAPO-5/0.9Si displays a lower density of Brønsted acid sites than SAPO-5/0.9Si, as also evidenced by ^1H MAS NMR (Table 5).

Proton transfer with more accessible Brønsted acid sites in hierarchical catalysts also occurs when 2,6-dTBP is adsorbed and a band at 1618 cm^{-1} (ν_{8a}), due to protonated 2,6-dTBPH$^+$ species,

can be clearly observed. Table 6 lists the density of accessible Brønsted acid sites (N) in HPSAPO-5/xSi catalysts titrated using 2,6-dTBP compared to the density of accessible sites titrated by NH_3. These data evidence that only a small fraction of Brønsted acid sites are accessible to the bulkier probe molecules. The accessibility factor (AF) [83], defined as the density of sites titrated by 2,6-dTBP divided by the density of Brønsted acid sites titrated by NH_3, reveals a higher value for HPSAPO-5/0.3Si (AF = 0.049), while HPSAPO-5/0.6Si and HPSAPO-5/0.9Si show a similar value (AF = 0.025).

By assuming that the Brønsted acid sites titrated by 2,6-dTBP are preferentially located on the mesoporous surface, we can estimate the density of Brønsted acid sites located in the micropores by subtracting the density of acid sites titrated by 2,6-dTBP from that titrated by NH_3. Interestingly, regardless of the Si loading, the density of Brønsted acid sites is similar in the different HPSAPO-5/xSi catalysts, with a value of 0.13 $\mu mol.m^{-2}$ or 0.08 sites.nm^{-2} of microporous surface area. In line with the results from ^1H MAS NMR, this observation points out that the density of Brønsted acid sites is not affected by the Si loading in the HPSAPO-5/xSi catalysts, and that a higher Si loading contributes

Table 6
Integrated area (A) of the δ_{asym} NH_4^+ (1450 cm^{-1}) and ν_{8a} 2,6-dTBPH$^+$ (1618 cm^{-1}) bands, density of accessible Brønsted sites (N), accessibility factor (AF) and density of acid sites in micropores measured using NH_3 and 2,6-dTBP probe molecules for HPSAPO-5/xSi catalysts with x = 0.3, 0.6 and 0.9.

x	NH_3 adsorption		2,6-dTBP adsorption		AF	Acid sites in micropores (μmol g^{-1}) [c]	SiOH density (sites/nm^2)[d]
	A[a] (cm^{-1})	N[b] ($\mu mol.g^{-1}$)	A[a] (cm^{-1})	N[b] (μmol g^{-1})			
0.3	6.29	42.8	1.04	2.1	0.049	40.7 (0.078)	0.04
0.6	6.80	46.2	0.58	1.2	0.025	45.1 (0.083)	0.13
0.9	6.66	45.3	0.58	1.2	0.025	44.2 (0.080)	0.14

[a] Integrated area A of the 1450 and 1618 cm^{-1} bands were obtained by using the spectra of the catalysts outgassed at 298 K to eliminate the contribution of physisorbed molecules.
[b] ε = 0.147 cm^2 μmol^{-1} [84] for NH_4^+ band and ε = 0.50 cm^2 μmol^{-1} [82].
[c] In parentheses, acid sites per nm^2 of microporous surface area (Table 4).
[d] SiOH sites (estimated on the basis of ^1H ss NMR abundances presented in Table 5) per nm^2 of mesoporous surface area (Table 4).

to the generation of Si-OH moieties at the expense of acid Si-O(H)-Al moieties for microporous SAPO-5/xSi, sitting mostly on the mesopores. Despite their different location on the catalyst, the interconnectivity of micro- and mesopores in the HPSAPO-5/xSi catalysts favors the cooperativity between the Brønsted acid sites and Si-OH groups during acid-catalyzed reactions, as recently unveiled by combining spectroscopic (inelastic neutron scattering, FTIR and MAS NMR) and computational analyses on HPSAPO-5/xSi catalysts [60]. This property is expected to facilitate the activation of MIBK and further attack to FF, catalyzing the aldol condensation/crotonization reaction (Scheme 3), considering also that the SiOH density is similar for HPSAPO-5/xSi catalysts with 0.6 and 0.9 Si content and it is low for HPSAPO-5/0.3Si (Table 6). In light of these considerations, the highest catalytic activity observed for HPSAPO-5/0.9Si can be attributed to the synergistic effect between the amount of OH sites and its hierarchical structure (highest mesoporous area and pore volume, Table 4).

The interaction of MIBK via H-bond with the Si-OH was confirmed by MIBK adsorption on the hierarchical catalysts, followed by FTIR spectroscopy. Upon MIBK adsorption (Fig. S17), the band ascribed to the O-H stretching of Si-OH groups (3745 cm^{-1}) vanishes, whereas characteristic bands attributed to the vibrational features of MIBK appear at lower wavenumbers. On the contrary, the bands ascribed to Brønsted acid sites (3630 and 3513 cm^{-1}) are visible, suggesting that Brønsted sites are still available. The shift of the C-O stretching mode of adsorbed MIBK with respect to that in liquid phase confirms that MIBK and SiOH interact by H-bonding (Table S2). We also measured FF adsorption after MIBK outgassing. Interestingly, the bands due to the O-H stretching of Brønsted sites completely disappear. However, the bands ascribed to Si-OH groups are visible, pointing out a preferential adsorption of FF in the micropores (Fig. S18). Overall, these results confirm the mechanism proposed in Scheme 3, encompassing the preferential adsorption of MIBK on the external SiOH groups.

3.6.3.3. NH$_3$-TPD profiles. NH$_3$-TPD measurements were also performed on the fresh and spent HPSAPO-5/0.9Si after the aldol condensation/crotonization reaction to gain a better insight into the density distribution and strength of acid sites (Fig. 8, Table S3 – entries 1 and 2). The NH$_3$-TPD profile of the fresh catalysts exhibits two main regions (Fig. 8A): (1) a low-temperature region (100–350 °C), and (2) a high-temperature region (450–650 °C). The first region can be deconvoluted into four bands (I-IV) that can be attributed to weakly acid sites in P-OH and Si-OH groups in line with the ^{27}Al, ^{31}P and ^{29}Si NMR MAS findings. Besides, NH$_4^+$.nNH$_3$ associations promoted by H-bonding cannot be excluded. The second region is constituted by a broad band (VI) that is indicative of strong acid sites and that, on the guidance of the FTIR spectra using
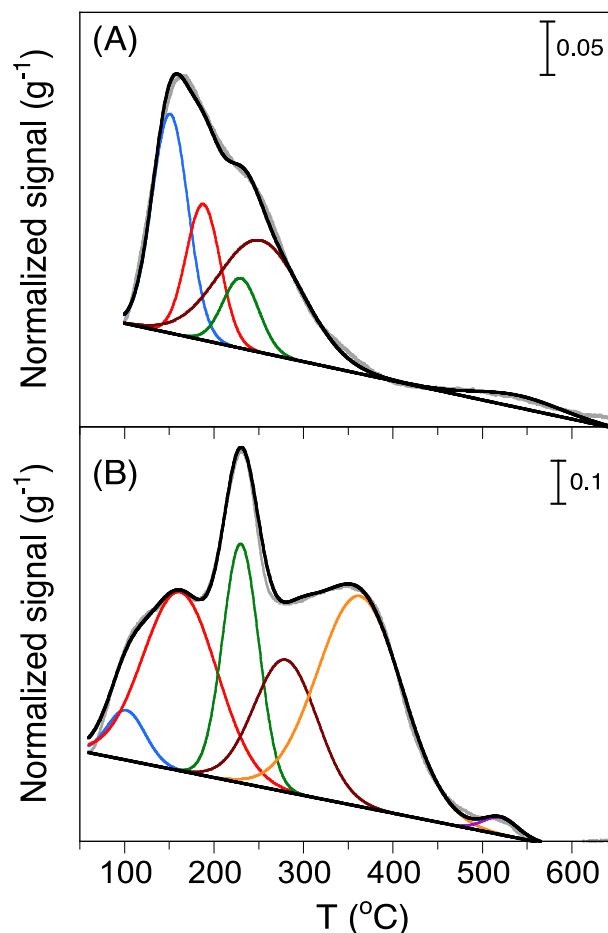

Fig. 8. NH$_3$-TPD profiles of (A) fresh and (B) spent HPSAPO-5/0.9Si catalysts. The peak deconvolution can be found in the SI (Table S2).

NH$_3$ as molecular probe, can be ascribed to Brønsted acid sites. By integrating the NH$_3$-TPD profile, the density of weak acid sites belonging to bands I-IV is 775 μmol.g^{-1}, whereas the density of strong acid sites is 32.7 μmol.g^{-1}. The latter value compares well with the density of sites measured by FTIR using NH$_3$ as probe molecule (45.3 μmol.g^{-1}), confirming that band VI can be assigned to strong Brønsted acid sites.

To further rationalize the higher activity of HPSAPO-5/0.9Si compared to reference acid catalysts, we measured the NH$_3$-TPD profiles for the series of catalysts listed in Table 1 (Figs. S21, S22A-B). ZrO$_2$ and ZnO exhibit bands mainly located in the low-temperature region (in blue), whereas the three acid zeolites (i.e.
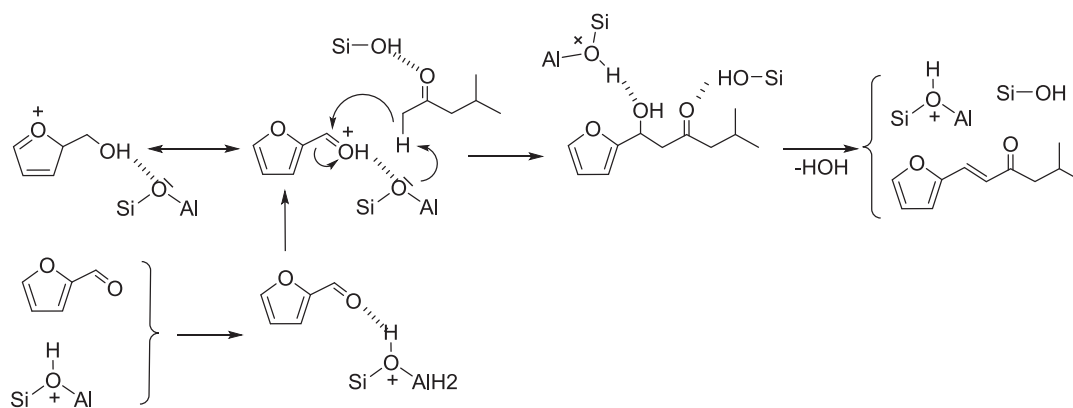
Scheme 3. Possible catalytic mechanism in the aldol condensation/crotonization reaction of FF with MIBK catalyzed by HPSAPO-5/0.9Si.

BEA, Y and MOR) also display bands in the high-temperature region (in red), but centered at a temperature lower than 550 °C. The deconvoluted NH_3-TPD profile of Al-SBA-15 shows three bands in the high-temperature region centered at 500 °C, 605 °C and 730 °C (Fig. S22C, Table S3 entry 4), being mainly attributed to Lewis acid centers [75]. These observations point out that strong Lewis acid centers are detrimental to the catalytic activity.

The key features of the NH_3-TPD profile on HPSAPO-5/0.9Si are essentially kept after the aldol condensation/crotonization reaction at 180 °C (Fig. 8B). Nonetheless, the low-temperature region expands to 450 °C due to the apparition of a new broad band (V) centered at 363 °C and a drastic decline of band I. The density of weak acid sites belonging to bands I-V is 1076 $\mu mol.g^{-1}$, which is larger than that of the fresh catalyst, pointing out the generation of additional weakly acid centers (band V) during the reaction. The generation of new acid centers can be attributed to partial hydroxylation of the external surface of HPSAPO-5/0.9Si during the reaction [85], resulting most likely in a preferential location near the micropore mouths not far from Al atoms. The presence of new weak acid centers is not expected to impact the catalytic activity and catalyst deactivation. In contrast, band VI ascribed to strong acid sites exhibits a slight decline from 32.7 to 12.7 $\mu mol.g^{-1}$, which can be attributed to partial blockage due to oligomers or coke species during the reaction as inferred by thermogravimetric analysys (TGA) (Fig. S19). Indeed, a characteristic weight loss is observed between 200 and 600 °C on the spent HPSAPO-5/0.9Si that can be attributed to the formation of aliphatic coke at the level of 160 mgC/g. The presence of partial catalyst deactivation can explain the presence of a plateau in the kinetic curves (Fig. 1) and selectivity-conversion plots (Fig. 2) for the ALD-1 selectivity at high conversion.

3.6.4. Nature of the Pd phase over HPSAPO-5/xSi

To gain insight into the Pd dispersion on HPSAPO-5/0.9Si, we visualized the 0.3%/HPSAPO-5/0.9Si and 4.8%/HPSAPO-5/0.9Si samples by HR-TEM (Fig. 9). In both cases, a high degree of Pd disper-

sion is observed with Pd nanoparticles smaller than 2.5 nm for 0.3%/HPSAPO-5/0.9Si, while two particle distributions centered at 5 nm and 14 nm are observed for 4.8%/HPSAPO-5/0.9Si. The H_2-TPR profiles revealed in both cases the presence of a reduction band centered at a temperature up to 60 °C, confirming the fast and complete reduction of the palladium phase in the one-pot reaction just upon introduction of H_2 to the reactor after ALD-1 formation.

We also measured the NH_3-TPD profile of the unreduced 4.8% Pd/HPSAPO-5/0.9Si catalyst (Fig. S20, Table S2 – entry 3). The key bands on the parent HPSAPO-5/0.9Si are essentially kept after Pd impregnation. However, bands I and II become more intense with a density of acid sites belonging to bands I-IV of 1163 $\mu mol.g^{-1}$ compared to 775 $\mu mol.g^{-1}$ for HPSAPO-5/0.9Si. This observation points out the generation of additional weakly acid centers upon palladium impregnation. In contrast, band VI ascribed to strong acid sites exhibits a slight shift to lower temperature (from 540 °C to 400 °C) together with an increase of the density of acid sites from 32.7 to 56.1 $\mu mol.g^{-1}$, which can be attributed to additional Lewis acidity ascribed to PdO. This additional acid site density vanishes upon reduction (not shown).

4. Conclusion

A series of crystalline silicoaluminophosphate SAPO-5 catalysts with hierarchical porosity and variable silicon content were synthesized using a bottom-up method starting from pre-synthesized MCM-41, with the surfactant (CTAB) inside the mesopores. In particular, HPSAPO-5/0.9Si catalyst exhibited a remarkable increase of the catalytic activity compared to the microporous counterpart in the aldol condensation/crotonization reaction between furfural and methyl isobutyl ketone.

HPSAPO-5/0.9Si exhibited a lower density of Brønsted acid centers compared to microporous SAPO-5/0.9Si, as inferred by combined ^1H MAS NMR and *in situ* FTIR spectroscopy using NH_3 as
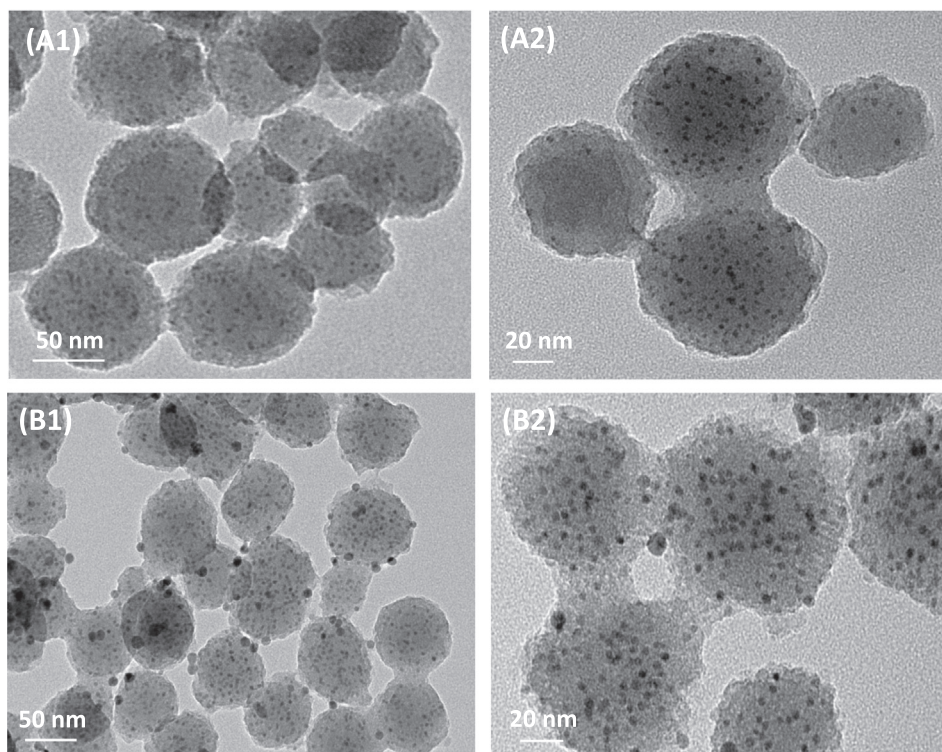

Fig. 9. HR-TEM micrographs of (A1,A2) 0.3%Pd/HPSAPO-5/0.9Si and (B1,B2) 4.8%Pd/HPSAPO-5/0.9Si.

probe molecule. However, HPSAPO-5/0.9Si displayed a higher mesoporous specific surface area combined with the presence of Si-OH moieties on the external surface. The interconnectivity of micro- and mesopores in HPSAPO-5/xSi catalysts is expected to favor the cooperativity between strong Brønsted acid sites located in the SAPO-5 channels, which are characterized by a band centered at 540 °C in the NH_3-TPD profile, and external Si-OH groups, facilitating the activation of MIBK and further attack to FF.

By impregnating Pd, 4.8%Pd/HPSAPO-5/0.9Si afforded the synthesis of hydrogenated THF-derivatives with 45% yield in the one-reactor tandem aldol condensation/crotonization reaction between furfural and methyl isobutyl ketone, followed by hydrogenation with molecular H_2. The catalytic activity declined after the reaction mostly due formation of carbon deposits, but could be recovered after calcination.

Declaration of Competing Interest

The authors declare that they have no known competing financial interests or personal relationships that could have appeared to influence the work reported in this paper.

Acknowledgements

Appendix A. Supplementary material

Supplementary data to this article can be found online at https://doi.org/10.1016/j.jcat.2021.03.003.

References

[1] M. Dusselier, M. Mascal, B.F. Sels, Top. Curr. Chem. 353 (2014) 1.
[2] D.M. Alonso, J.Q. Bond, J.A. Dumesic, Green Chem. 12 (2010) 1493.
[3] P. Anastas, N. Eghbali, Chem. Soc. Rev. 39 (2010) 301.
[4] A.A. Koutinas, C. Du, R.H. Wang, C. Webb, Introduction to Chemicals from Biomass, Wiley, Hoboken, 2008, p. 77.
[5] Y. Ogiwara, T. Uchiyama, N. Sakai, Angew. Chem. Int. Ed. 55 (2016) 1864.
[6] R. Mariscal, P. Maireles-Torres, M. Ojeda, I. Sádaba, M. López Granados, Energy Environ. Sci. 9 (2016) 1144.
[7] R.J. van Putten, J.C. van der Waal, E. de Jong, C.B. Rasrendra, H.J. Heeres, J.G. de Vries, Chem. Rev. 113 (2013) 1499.
[8] X. Li, P. Jia, T. Wang, ACS Catal. 6 (2016) 7621–7640.
[9] T. Werpy, G. Petersen, (Eds.), Top Value Added Chemicals from Biomass, U.S. Department of Energy (DOE) report: DOE/GO-102004-1992, 2004.
[10] L. Hu, L. Lin, S. Liu, Ind. Eng. Chem. Res. 53 (2014) 9969.
[11] L. Bui, H. Luo, W.R. Gunther, Y. Roman-Leshkov, Angew. Chem. Int. Ed. 52 (2013) 8022.
[12] M. Kim, Y. Su, A. Fukuoka, E.J.M. Hensen, K. Nakajima, Angew. Chem. Int. Ed. 57 (2018) 8235.
[13] N. Alonso-Fagúndez, M.L. Granados, R. Mariscal, M. Ojeda, ChemSusChem. 5 (2012) 1984.
[14] G. Li, N. Li, Z. Wang, C. Li, A. Wang, X. Wang, Y. Cong, T. Zhang, ChemSusChem. 5 (2012) 1958.
[15] A. Corma, O. de la Torre, M. Renz, N. Villandier, Angew. Chem. Int. Ed. 50 (2011) 2375.
[16] A.D. Sutton, F.D. Waldie, R. Wu, M. Schlaf, L.A. 'Pete' Silks III, J.C. Gordon, Nat. Chem. 5 (2013) 428–432.
[17] G.W. Huber, S. Iborra, A. Corma, Chem. Rev. 106 (2006) 4044.
[18] G.W. Huber, J.N. Chheda, C.J. Barrett, J.A. Dumesic, Science 308 (2005) 1446–1450.
[19] J. Xu, L. Li, G. Li, A. Wang, Y. Cong, X. Wang, N. Li, A.C.S. Sust, Chem. Eng. 6 (2018) 6126–6134.
[20] C.J. Barrett, J.N. Chheda, G.W. Huber, J.A. Dumesic, Appl. Catal. B: Envion. 66 (2006) 111–118.
[21] R. Xing, A.V. Subrahmanyam, H. Olcay, W. Qi, G.P. van Walsum, H. Pendse, G. W. Huber, Green Chem. 12 (2010) 1933–1946.
[22] J. Yang, N. Li, G. Li, W. Wang, A. Wang, X. Wang, Y. Cong, T. Zhang, ChemSusChem 6 (2013) 1149–1152.
[24] B. Pholjaroen, N. Li, J. Yang, G. Li, W. Wang, A. Wang, Y. Cong, X. Wang, T. Zhang, Ind. Eng. Chem. Res. 53 (2014) 13618–13625.
[29] H. Chang, A. Hussain Motagamwala, G.W. Huber, J.A. Dumesic, Green Chem. 21 (2019) 5532–5540.
[30] H.J. Cho, D. Kim, J. Li, D. Su, B. Xu, J. Am. Chem. Soc. 140 (2018) 13514–13520.
[31] S. Jiang, E. Muller, M. Pera-Titus, F. Jerôme, K. De Oliveira Vigier, ChemSusChem. 13 (2020) 1699–1704.
[32] S. Jiang, C. Ma, E. Muller, M. Pera-Titus, F. Jerome, K. De Oliveira Vigier, ACS Catal. 10 (2019) 8893–8902.
[33] W. Shen, G.A. Tompsett, K.D. Hammond, R. Xing, F. Dogan, C.P. Grey, W. Curtis Conner Jr, S.M. Auerbach, G.W. Huber, Appl. Catal. A: Gen. 392 (2011) 57–68.
[34] I. Sádaba, M. Ojeda, R. Mariscal, R. Richards, M. López Granados, Catal. Today 167 (2011) 77–83.
[35] I. Sádaba, M. Ojeda, R. Mariscal, J.L.G. Fierro, M. López Granados, Appl. Catal. B: Environ. 101 (2011) 638–648.
[36] L. Faba, E. Díaz, S. Ordónez, Appl. Catal. B: Environ. 113–114 (2012) 201–211.
[37] D. Nguyen Thanh, O. Kikhtyanin, R. Ramos, M. Kothari, P. Ulbrich, T. Munshi, D. Kubicka, Catal. Today 277 (2016) 97–107.
[38] O. Kikhtyanin, R. Bulanek, K. Frohlich, J. Cejka, D. Kubicka, J. Mol. Catal. A: Gen. 424 (2016) 358–368.
[39] O. Kikhtyanin, Y. Ganjkhanlou, D. Kubicka, R. Bulanek, J. Cejka, Appl. Catal. Gen. 549 (2018) 8–18.
[40] A. Philippou, M.W. Anderson, J. Catal 189 (2000) 395–400.
[41] G. Liang, A. Wang, X. Zhao, N. Lei, T. Zhang, Green Chem. 18 (2016) 3430–3438.
[42] O. Kikhtyanin, V. Kelbichova, D. Vitvarova, M. Kubu, D. Kubicka, Catal. Today 227 (2014) 154–162.
[43] O. Kikhtyanin, P. Chlubna, T. Jindrova, D. Kubicka, Dalton Trans. 43 (2014) 10628–10641.
[44] J. Cueto, V. Korobka, L. Faba, E. Diaz, S. Ordonez, A.C.S. Sust, Chem. Eng. 8 (2020) 4371–4383.
[45] O. Kikhtyanin, D. Kubicka, J. Cejka, Catal. Today 243 (2015) 158–162.
[46] D. Verboekend, J. Perez-Ramírez, Catal, Sci. Technol. 1 (2011) 879–890.
[47] J. Aguado, J. Sotelo, D. Serrano, J. Calles, J. Escola, Energy Fuels 11 (1997) 1225–1231.
[48] V.L. Zholobenko, A.Y. Khodakov, D. Durand, Micropor. Mesopor. Mater. 66 (2003) 297–302.
[49] X. Zhu, J.P. Hofmann, B. Mezari, N. Kosinov, L. Wu, Q. Qian, B.M. Weckhuysen, S. Asahina, J. Ruiz-Martinez, E.J.M. Hensen, ACS Catal. 6 (2016) 2163–2177.
[50] R. Ramos, J.M. Hidalgo, M. Göpel, Z. Tisler, F. Bertella, A. Martinez, O. Kikhtyanin, D. Kubicka, Catal. Commun. 114 (2018) 42–45.
[51] M. Su, W. Li, Q. Ma, S. Li, T. Yang, X. Dou, Energy Fuels 33 (2019) 12518–12526.
[52] A. Al-Ani, C. Freitas, V. Zholobenko, Micropor. Mesopor. Mater. 293 (2020) 109805.
[53] M. Hartmann, L. Kevan, Chem. Rev. 99 (1999) 635–664.
[54] E. Gianotti, M. Manzoli, M.E. Potter, V.N. Shetti, D. Sun, J. Paterson, T.M. Mezza, A. Levy, R. Raja, Chem. Sci. 5 (2014) 1810–1819.
[55] R.J. Pellet, G.N. Long, J.L. Rabo, P.K. Coughlin, US 4,751,340, 1988.
[56] R.J. Pellet, G.N. Long, J.L. Rabo, P.K. Coughlin, US 4,740,650, 1988.
[57] D. Verboekend, M. Milina, J. Perez-Ramirez, Chem. Mater. 26 (2014) 4552–4562.
[58] D. Jadav, R. Bandyopadhyay, M. Bandyopadhyay, Eur. J. Inorg. Chem. (2020) 847–853.
[59] C. Wang, M. Yang, P. Tian, S. Xu, Y. Yang, D. Wang, Y. Yuan, Z. Liu, Dual template-directed synthesis of SAPO-34 nanosheet assemblies with improved stability in the methanol to olefins reaction, J. Mater. Chem. A 3 (2015) 5608–5616.
[60] S.H. Newland, W. Sinkler, T. Mezza, S.R. Bare, M. Caravetta, I.M. Haies, A. Levy, S. Keenan, R. Raja, ACS Catal. 5 (2015) 6587–6593.
[61] S. Chapman, A.J. O'Malley, I. Miletto, M. Carravetta, P. Cox, E. Gianotti, L. Marchese, S.F. Parker, R. Raja, Chem. Eur. J. 25 (2019) 9938–9947.
[62] I. Miletto, G. Paul, S. Chapman, G. Gatti, L. Marchese, R. Raja, E. Gianotti, Chem. Eur. J. 23 (2017) 9952–9961.
[63] N. Danilina, F. Krumeich, J.A. van Bokhoven, J. Catal. 272 (2010) 37–44.
[64] S. Chapman, M. Carravetta, I. Miletto, C.M. Doherty, H. Dixon, J.D. Taylor, E. Gianotti, J. Yu, R. Raja, Angew. Chem. Int Ed. 59 (2020) 2–11.
[65] J.A. Rabo, G.A. Gajda, Catal. Rev. Sci. Eng. 31 (1989) 385–430.
[66] B.M. Lok, C.A. Messina, R.L. Patton, R.T. Gajek, T.R. Cannan, E.M. Flanigen, J. Am. Chem. Soc. 106 (1984) 6092–6093.
[67] J.A. Rabo, In E.G. Derouane, F. Lemos, C. Naccache, F. R. Ribeiro, (Eds.) Zeolite Microporous Solids: Synthesis, Structure and Reactivity, NATO ASI Ser. C 352, 1992, p. 531.
[68] G. Sastre, D.W. Lewis, C.R.A. Catlow, J. Phys. Chem. B 101 (1997) 5249–5262.
[69] C.J. Brinker, Y. Lu, A. Sellinger, H. Fan, Adv. Mater. 11 (1999) 579–585.
[70] M. Thommes, K.A. Cychosz, Adsorption 20 (2014) 233–250.
[71] M. Errahali, G. Gatti, L. Tei, G. Paul, G.A. Rolla, L. Canti, A. Fraccarollo, M. Cossi, A. Comotti, P. Sozzani, L. Marchese, J. Phys. Chem. C 118 (2014) 28699–28710.
[72] K.A. Cychosz, R. Guillet-Nicolas, J. Garcia, M. Thommes, Chem. Soc. Rev. 46 (2017) 389–414.
[73] G.V.A. Martins, G. Berlier, C. Bisio, S. Coluccia, H.O. Pastore, L. Marchese, J. Phys. Chem. C 112 (2008) 7193–7200.
[74] F. Jing, B. Katryniok, M. Araque, R. Wojcieszak, M. Capron, S. Paul, M. Daturi, J.-M. Clacens, F. De Campo, A. Liebens, F. Dumeignil, M. Pera-Titus, Catal, Sci. Technol. 6 (2016) 5830–5840.
[75] F. Jing, B. Katryniok, S. Paul, L. Fang, A. Liebens, B. Hu, F. Dumeignil, M. Pera-Titus, ChemCatChem. 9 (2017) 258–262.

[76] W. Lai, S. Yang, Y. Jiang, F. Zhao, Z. Li, B. Zaman, M. Fayaz, X. Li, Y. Chen, Adsorption 26 (2020) 633–644.

[77] B. Zibrowius, E. Loffler, M. Hunger, Zeolites 12 (1992) 167–174.

[78] J. Chen, P.A. Wright, S. Natarajan, J.M. Thomas, Stud. Surf. Sci. Catal. 843 (1994) 1731–1738.

[79] S.I. Lee, H.J. Chon, Chem. Soc., Faraday Trans. 93 (1997) 1855–1860.

[80] G. Müller, J. Bodis, G. Eder-Mirth, J. Kornatowski, J.A. Lercher, J. Mol. Struct. 410–411 (1997) 173–178.

[81] C.V. Hidalgo, H. Itoh, T. Hattori, N. Niwa, Y. Murakami, J. Catal. 85 (1984) 362–369.

[82] K. Gòra-Merek, K. Tarach, M. Choi, J. Phys. Chem. C 118 (2014) 12266–12274.

[83] K. Sadowska, K. Gorà-Marek, J. Datka, J. Phys. Chem. C 117 (2013) 9237–9244.

[84] J. Datka, B. Gil, A. Kubacka, Zeolites 15 (1995) 501–506.

[85] B.M. Lok, B.K. Marcus, C.L. Angell, Zeolites 6 (1986) 185–194.

[86] S.G. Wettstein, D.M. Alonso, Y. Chong, J.A. Dumesic, Energy Environ. Sci. 5 (2012) 8199–8203.

[87] L. Faba, E. Diaz, S. Ordonez, ChemSusChem 7 (2014) 2816–2820.

[88] C. Ki, D. Ding, Q. Xia, Y. Wang, ChemSusChem 9 (2016) 1712–1718.

[89] L. Faba, E. Diaz, S. Ordonez, Catal. Today 164 (2011) 451–456.

[90] M. Li, X. Xu, Y. Gong, Z. Wei, Z. Hou, H. Li, Y. Wang, Green Chem. 16 (2014) 4371–4377.